JACS
JOURNAL OF THE AMERICAN CHEMICAL SOCIETY

Article

pubs.acs.org/JACS

Revealing the Mechanisms behind SnO_2 Nanoparticle Formation and Growth during Hydrothermal Synthesis: An In Situ Total Scattering Study

Kirsten M. Ø. Jensen,[†] Mogens Christensen,[†] Pavol Juhas,[‡] Christoffer Tyrsted,[†] Espen D. Bøjesen,[†] Nina Lock,[†] Simon J. L. Billinge,*[,‡,§] and Bo B. Iversen*[,†]

[†]Center for Materials Crystallography, Department of Chemistry and iNANO, Aarhus University, DK-8000 Aarhus C, Denmark

[‡]Applied Physics and Applied Mathematics, Columbia University, New York, New York 10027, United States

[§]Condensed Matter Physics and Materials Science Department, Brookhaven National Laboratory, Upton, New York 11973, United States

Supporting Information

ABSTRACT: The formation and growth mechanisms in the hydrothermal synthesis of SnO_2 nanoparticles from aqueous solutions of $SnCl_4 \cdot 5H_2O$ have been elucidated by means of in situ X-ray total scattering (PDF) measurements. The analysis of the data reveals that when the tin(IV) chloride precursor is dissolved, chloride ions and water coordinate octahedrally to tin(IV), forming aquachlorotin(IV) complexes of the form $[SnCl_x(H_2O)_{6-x}]^{(4-x)+}$ as well as hexaaquatin(IV) complexes $[Sn(H_2O)_{6-y}(OH)_y]^{(4-y)+}$. Upon heating, ellipsoidal SnO_2 nanoparticles are formed uniquely from hexaaquatin(IV). The nanoparticle size and morphology (aspect ratio) are dependent on both the reaction temperature and the precursor concentration, and particles as small as ~2 nm can be synthesized. Analysis of the growth curves shows that Ostwald ripening only takes place above 200 °C, and in general the growth is limited by diffusion of precursor species to the growing particle. The *c*-parameter in the tetragonal lattice is observed to expand up to 0.5% for particle sizes down to 2−3 nm as compared to the bulk value. SnO_2 nanoparticles below 3−4 nm do not form in the bulk rutile structure, but as an orthorhombic structural modification, which previously has only been reported at pressures above 5 GPa. Thus, adjustment of the synthesis temperature and precursor concentration not only allows control over nanoparticle size and morphology but also the structure.

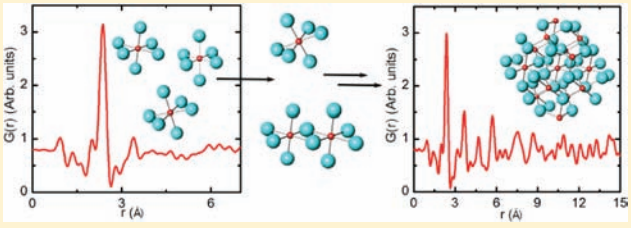

INTRODUCTION

It is well established that the material properties of metal and metal oxide nanoparticles are highly dependent on the particle characteristics such as size, shape, and aggregation structure.[1−4] In the development of advanced functional nanomaterials, finding a green and energy efficient synthesis pathway, which allows control over these characteristics, is therefore crucial. In this context, the hydrothermal method is promising, and during the past decades various inorganic micro- and nanoparticles of high crystallinity and homogeneity have been produced using this approach. It has been shown that many of the particle characteristics can be altered by adjusting simple synthesis parameters such as temperature, pressure, precursor concentration, and reaction time.[5] However, the mechanisms controlling particle formation and growth during hydrothermal synthesis are still not fully understood, and to produce nanoparticles with tailor-made characteristics, it is necessary to gain further insight into the processes. We have in a number of studies used X-ray scattering techniques to investigate in situ the hydrothermal synthesis of various inorganic compounds, that is, watching the formation and growth of nanoparticles as it takes place.[6−14]

Here, we use in situ total scattering with a time resolution of few seconds in the study of the hydrothermal synthesis of SnO_2, a large gap n-type semiconductor. So far, only a few studies have used the total scattering technique to obtain information about chemical reactions as they happen,[15−20] and none of these have taken place under hydrothermal conditions. Total scattering and pair distribution function (PDF) analysis, as opposed to conventional crystallographic diffraction methods, allow extraction of structural information from amorphous, nanosized structures as well as crystalline structures because information on both the short- and the long-range order can be obtained.[21,22] The PDF analysis therefore allows for deeper insight into processes taking place during crystallization.

In recent years, SnO_2 nanoparticles have been studied extensively for several applications. In 1997, Idota et al. first introduced Sn-based anode materials for Li-ion batteries,[23] and, apart from being a promising anode material,[24−27] SnO_2 is used in numerous other applications, for example, as a gas sensor,[28]

Received: January 30, 2012
Published: March 15, 2012

dx.doi.org/10.1021/ja300978f | J. Am. Chem. Soc. 2012, 134, 6785−6792

photo catalyst, and thermoelectric material.[29] Several studies of the hydrothermal synthesis of SnO_2 have been published,[30−35] and for many applications hydrothermally synthesized particles show superior properties to materials synthesized using high temperature methods.[31,36−38] Here, we use total scattering to reveal the mechanisms behind particle formation and growth.

EXPERIMENTS AND DATA ANALYSIS METHODS

The SnO_2 nanoparticles were crystallized from aqueous solutions of $SnCl_4{\cdot}5H_2O$ (Sigma-Aldrich, 98%) of various concentrations (1, 2, and 4 M). The in situ total scattering measurements were performed at the 11-ID-B beamline at APS, Argonne National Laboratory, U.S. The experimental setup is sketched in Figure 1 and has been described in detail

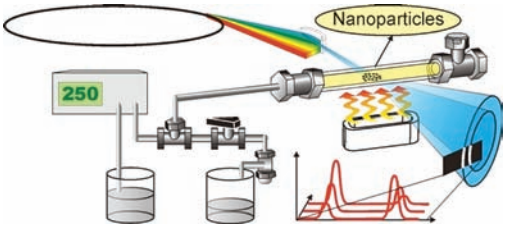

Figure 1. Experimental setup. The synchrotron X-ray beam is monochromatized, hits the nanoparticles inside the reactor, and gets scattered onto the 2D detector. The reactor is heated by a jet of hot air and pressurized by water.

elsewhere.[39] The precursor is injected into the reactor, which consists of a thin fused silica tube measuring 0.7 mm in inner diameter and 0.09 mm in wall thickness, ensuring a high transmission of X-rays. The tube is mounted in the setup using Swagelok fittings, pressurized with deionized water, and heated using a jet of hot air coming from below the sample. At the same time as the experiment is initiated by turning on the heating, sequential X-ray exposures are started. The efficiency of the heater combined with the small volume of the capillary ensures very fast heating, and the desired temperature is reached within seconds after initiation of the experiment. For all experiments, the pressure was set to 250 bar, whereas the temperature was varied between 160 and 350 °C. A Perkin-Elmer amorphous silicon detector measuring 40 × 40 cm^2 was placed 226 mm from the sample. The X-ray wavelength was 0.212 Å, and q-max was ∼21 $Å^{-1}$. The time resolution of the data was 7 s.

The raw total scattering data were integrated in Fit2D,[40] and the PDFs were subsequently obtained using PDFgetX3 (unpublished). Scattering from the capillary with deionized water at the appropriate conditions was subtracted from the integrated pattern before using data in the q-range from 0.6 to 19.5 $Å^{-1}$ in the Fourier transformation. The PDFs were modeled to extract structural and microstructural parameters using SrFit (unpublished) and PDFgui.[41] Furthermore, the data were analyzed by Rietveld refinement using the FullProf Suite.[42]

Synchrotron powder X-ray diffraction (PXRD) experiments were also performed at beamline i711 at MAXII, MAX-lab, Sweden, using the same experimental setup. For these experiments, the pressure was again fixed at 250 bar, whereas the temperature was varied from 160 to 250 °C. Experiments using both 1 and 2 M precursor were done. The PXRD data were integrated using Fit2D[40] and treated by single peak fitting. The wavelength was 1.00 Å, and the detector-to-sample distance was 79.12 mm. The detector was an Oxford Diffraction Titan CCD measuring 16.5 cm in diameter. The time resolution of the data was 4 s, and q_{max} was 3.8 $Å^{-1}$.

Nanoparticles synthesized in the same reactor in our home laboratory using 2 M $SnCl_4{\cdot}5H_2O$ (Sigma-Aldrich, 98%) at 250 °C and 250 bar for 5 min were used for ex situ TEM characterization. The TEM characterization was done using a Phillips model CM20 TEM microscope working at 200 kV. Because of inhomogeneous heating of the capillary when moving away from the center of the tube, care has to be taken when comparing X-ray data collected from the center of the reactor with TEM data measured on material collected from the entire hot zone of the reactor.

RESULTS AND DISCUSSION

Structures in Aqueous Solutions of $SnCl_4$. Figure 2A shows room-temperature total scattering data from the precursor at different concentrations. It is clear that the concentration of $SnCl_4$ dramatically affects the scattering pattern. The structural differences can be understood by considering the reduced pair distribution functions (PDF) shown in Figure 2B. In the data for the 2 and 4 M $SnCl_4$ solutions, a large peak is present at $r \approx 2.4$ Å along with several smaller peaks at ∼3.3 Å. These features agree well with the formation of $[SnCl_x(H_2O)_{6-x}]^{(4-x)+}$ complexes, which has been reported in NMR studies of $SnCl_4$ solutions.[43] Sn^{4+} and Cl^- have Shannon ionic radii of 0.55 and 1.81 Å, respectively, giving

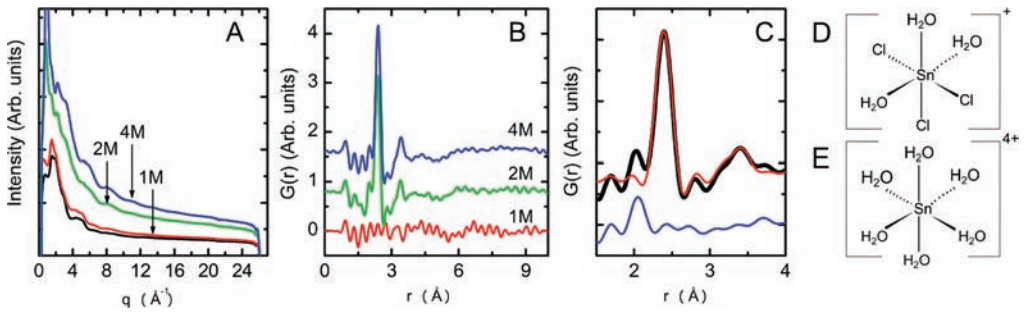

Figure 2. (A) Raw total scattering data from 1 M (red), 2 M (green), and 4 M (blue) solutions of $SnCl_4{\cdot}5H_2O$ at room temperature. The scattering pattern from the capillary filled with water is shown in black, almost overlapped by the pattern from the 1 M solution. (B) PDFs obtained from the data shown in (A). The scattering pattern from water has been subtracted prior to the Fourier transformation. (C) Fit of *mer*-$[SnCl_3(H_2O)_3]$ to data recorded of 2 M $SnCl_4$ at room temperature. The thick black curve shows the observed $G(r)$, the red curve the model, and the blue the difference between the two. (D) *mer*-Triaquatrichlorotin(IV). (E) Hexaaquatin(IV).

dx.doi.org/10.1021/ja300978f | J. Am. Chem. Soc. 2012, 134, 6785−6792

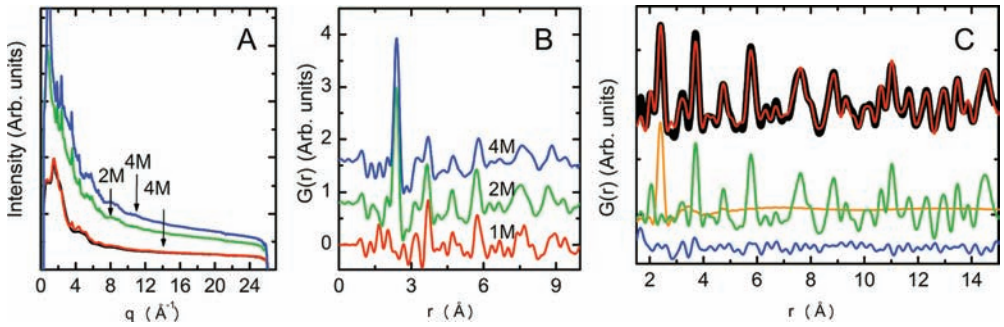

Figure 3. (A) Raw total scattering data from 1 M (red), 2 M (green), and 4 M (blue) solutions of $SnCl_4 \cdot 5H_2O$ after 6 min at 200 °C. The black line shows the total scattering from the capillary filled with water at 200 °C. (B) PDFs obtained from the data shown in (A), using the same color codes. (C) Fit to the $G(r)$ obtained after 30 min at 250 °C, 2 M. The observed $G(r)$ is shown by the thick black line, with the calculated in red. The contribution from the $[SnCl_3(H_2O)_3]^+$ is shown in orange and from SnO_2 in green. The blue line in the bottom of the graph is the difference between the total calculated $G(r)$ and the observed $G(r)$.

Sn−Cl bond lengths of ca. 2.36 Å,[44] that is, close to the *r*-value for the most intense peak.

A model describing the complex was applied as shown in Figure 2C. The NMR study of $SnCl_4$ solutions showed formation of several species with different stoichiometries such as $[SnCl_4(H_2O)_2]$ and $[SnCl_3(H_2O)_3]^+$ in different quantities.[43] However, to reduce the number of parameters, only one complex was included in the final model, *mer*-$[SnCl_3(H_2O)_3]^+$ (Figure 2D), which has the weighted average stoichiometry of the species reported in 2 M $SnCl_4$ solution.[43] To simplify the model, H_2O was replaced by O. The refinement of the model gave Sn−Cl and Sn−O distances of 2.42 and 2.26 Å, respectively, which agrees well with single-crystal diffraction studies of *cis*-$[SnCl_4(H_2O)_2]$ reporting Sn−Cl distances of 2.37−2.43 Å and Sn−O distances between 2.15 and 2.30 Å.[45] The shoulder at ∼2.02 Å does not originate from the aquachlorotin(IV) complex, but can be ascribed to the Sn−O distances in $[Sn(OH_2)_6]^{4+}$ (Figure 2E), which is believed to form simultaneously with $[SnCl_x(H_2O)_{6-x}]^{(4-x)+}$ species. Sn^{4+} is a Lewis acid, and hexaaquatin(IV) is therefore partially deprotonated, yielding an acidic solution and complexes of the type $[Sn(H_2O)_{6-y}(OH)_y]^{(4-y)+}$.

No significant structural features from either complex are seen in the PDF from the 1 M solution. This is most likely due to the relatively low concentration of the precursor, which makes the scattering signal from Sn species insignificant as compared to that of the water in the capillary.

Formation of SnO_2 Nanoparticles. In Figure 3A are shown the raw data collected after 6 min at 200 °C, and Bragg peaks from crystalline SnO_2 nanoparticles are clearly visible. Figure 3B shows the PDFs obtained from the total scattering in Figure 3A. Here, all significant peaks above r = 3.5 Å can be ascribed to the rutile SnO_2 structure; however, for the 2 and 4 M experiments, the Sn−Cl peak is still present, and it remains in the PDF throughout all experiments performed with the high precursor concentrations.

The metal complexes present in the precursor solution are the building blocks for the SnO_2 nanoparticles, and the precise formation mechanism was elucidated by modeling the PDFs of *mer*-$[SnCl_3(H_2O)_3]^+$ and the SnO_2 nanoparticles simultaneously, as is illustrated in Figure 3C. In the modeling of the time-resolved data, the scale factor for *mer*-$[SnCl_3(H_2O)_3]^+$ was refined along with the bond distances and the anisotropic thermal parameters for the ligands. These were restrained such that the factors expressing the vibrations along the bond (longitudinal) were all constrained to take the same value, u_l, and all vibrations perpendicular to the bond (transverse) were constrained to one value, u_t. For the crystalline phase, the scale factor, the unit cell, the atomic positions, and the isotropic thermal parameters were refined. Additional examples of the fits are shown in the Supporting Information along with the resulting parameters.

The time- and temperature-dependent scale factors obtained from the modeling are plotted in Figure 4A. In the beginning of

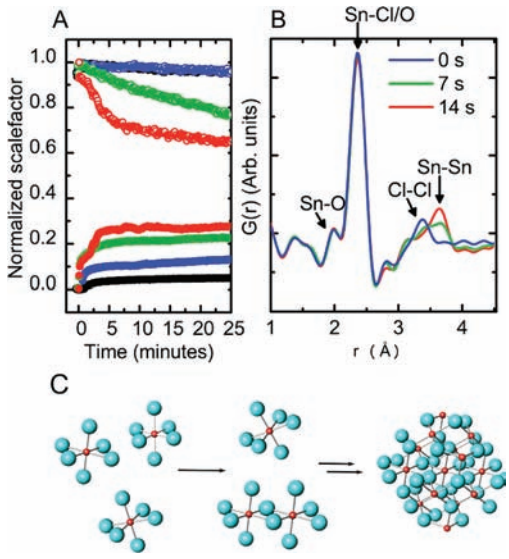

Figure 4. (A) Normalized scale factors for the complex (open symbols) and SnO_2 (closed symbols). Black symbols show the data for 2 M and 160 °C, blue 2 M and 200 °C, green 2 M and 250 °C, and red 2 M and 350 °C. (B) $G(r)$ calculated from the three first frames of the experiment done at 200 °C and 2 M. (C) Formation mechanism for SnO_2 nanoparticles, where Sn^{4+} is shown as red, and O^{2-} as blue. H^+ is not shown. $[Sn(H_2O)_{6-y}(OH)_y]^{(4-y)+}$ units cluster together and form SnO_2 nanoparticles of the rutile structure, where Sn is octahedrally coordinated.

the reaction, the SnO_2 scale factor rapidly increases, but interestingly a similar decrease in the value for the aquachlorotin(VI) complex scale factor is not observed. This is also evident in the PDFs obtained for the first few frames after the initiation of the experiment, as shown in Figure 4B, where the intensity of the Sn−Sn peak at ca. 3.68 Å increases significantly more than the Sn−Cl intensity at 2.36 Å decreases. This shows that the SnO_2 nanoparticles do not form directly

dx.doi.org/10.1021/ja300978f | J. Am. Chem. Soc. 2012, 134, 6785−6792

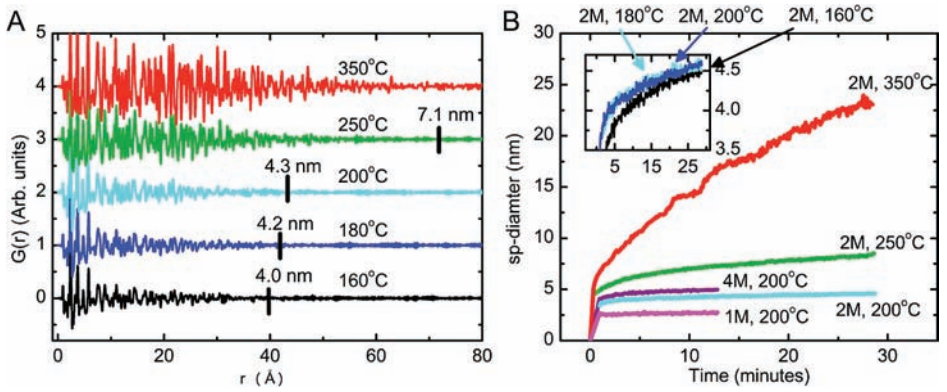

Figure 5. (A) $G(r)$s obtained from the frames recorded after 10 min for the experiments performed with 2 M precursor. The refined sp-diameter is marked by the black ticks. (B) The sp-diameters plotted as function of time for all experiments. The insert shows the size region from 3.5 to 4.5 nm. The growth curves from the three experiments done at 160, 180, and 200 °C with 2 M are almost completely overlapping.

from the Sn^{4+} ions bound in the chloride complex, but from Sn^{4+} ions coordinated in the hexaaquatin(IV) complex. The Sn−O peak at 2.02 Å remains constant in intensity as SnO_2 nanoparticles form, and indeed the Sn−O bond length in the crystalline SnO_2 refines to an identical bond length value. Overall, the data conclusively show that the SnO_2 nanoparticles must form from clustering of octahedrally coordinated aquahydroxotin(IV) complexes as illustrated in Figure 4C, and the formation mechanism can be written as:

$$[Sn(H_2O)_{6-y}(OH)_y]^{(4-y)+}(aq) \rightarrow SnO_2(s) + yH_2O(l) + (4-y)H_3O^+(aq)$$

As the reaction progresses, that is, as the aquahydroxotin(IV) units form solid SnO_2, aquachlorotin(IV) slowly disproportionates, causing more and more tin to form SnO_2 as is seen in the gradual decrease of the *mer*-$[SnCl_3(H_2O)_3]$ scale factor. The Cl−Cl peak at 3.32 broadens as the heating is initiated and can subsequently no longer be distinguished from the SnO_2 peaks. The broadening of the peak is due to strong thermal vibrations of the ligands transverse to the Sn−ligand bond. This is discussed in further detail in the Supporting Information.

Growth of Nanocrystalline SnO_2. The spatial extent of the correlations in the PDF provides information about the growth of the nanoparticles as illustrated by the $G(r)$ in Figure 5A. The data shown were all recorded after 10 min with the 2 M precursor at different temperatures. It is clear that increasing the synthesis temperature extends the PDF oscillations to larger r-values. However, to get an estimate of the particle size, the instrumental resolution has to be taken into account, because this dampens the oscillations at high r and causes them to completely disappear above 60 Å. Therefore, both the instrument effect and the particle size were included in the model. Examples of the fits along with the resulting parameters and estimated standard deviations are given in the Supporting Information. The resulting spherical particle diameters (sp-diameter parameter) are shown in Figure 5B.

The results for the 2 M experiments clearly reveal that it is possible to control the particle size by means of the reaction temperature. This is seen when comparing the growth curves obtained from the 200, 250, and 350 °C syntheses. However, below 200 °C, the particle size is not temperature dependent and appears to be stable around 4 nm, as shown in the inset in Figure 5B. The effect of $SnCl_4$ concentration on particle size can be seen when comparing the growth curves from the syntheses done using 1, 2, and 4 M at a reaction temperature of 200 °C. With increasing precursor concentration, the particles grow larger, and to synthesize very small particles (<4 nm), the $SnCl_4$ concentration should be reduced to 1 M or less. Note that for the experiment done at 350 °C with 2 M precursor, particle sizes well above the instrumental resolution limit are obtained, and for these values the uncertainties are significant.

The growth mechanisms at different temperatures can be understood when considering the increase in particle volume along with the total amount of SnO_2 nanoparticles formed. The volumes of the particles, calculated as $V = (sp)^3$, are plotted with the scale factors in Figure 6. For the 180 °C experiments,

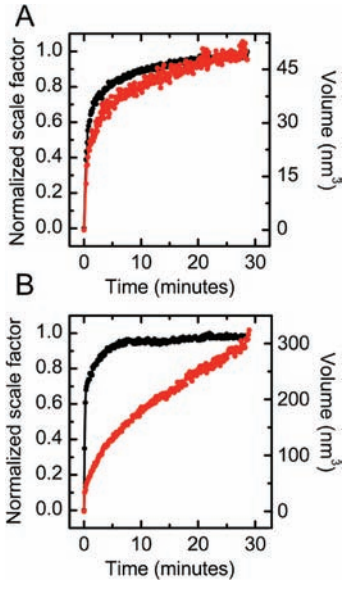

Figure 6. Normalized scale factor (black) plotted with the particle volume (red). (A) 180 °C, 2 M; (B) 250 °C, 2 M.

the growth curves and scale factors follow exactly the same path; that is, the particles grow because more SnO_2 can be formed from hexaaquatin(IV). The same behavior is observed for 160 and 200 °C (see Supporting Information). However, at 250 °C, the scale factor first increases rapidly, and then stabilizes after ca. 5 min. After the stabilization of the scale factor, the particle volume continues to increase, indicating particle growth by Ostwald ripening. This explains the different

dx.doi.org/10.1021/ja300978f | J. Am. Chem. Soc. 2012, 134, 6785−6792

dependency of the particle size on temperature below and above 200 °C.

The data were also treated by Rietveld refinement, and details are given in the Supporting Information. In q-space, the particle growth can be studied by applying the Scherrer equation,[46] stating that the peak width is related to the volume weighted size of the coherently diffraction domains, that is, crystallites, although this becomes unreliable for very small particle sizes. The Rietveld fits improve when the particles are allowed to elongate along the c-axis; that is, the particles are not spherical. Despite underestimating the absolute crystallite size as compared to the PDF, the Rietveld refined anisotropy should be reliable. The refined volume weighted particle sizes are shown in Figure 7A and B. The aspect ratio between the sizes

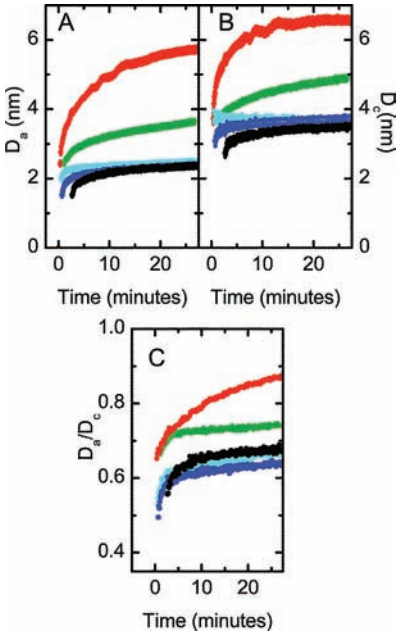

Figure 7. (A) Volume weighted crystallite sizes along the crystallographic a/b direction, obtained from Rietveld refinement. (B) Volume weighted crystallite sizes along the c direction. (C) Crystallite aspect ratio (D_a/D_c). All results shown are from the 2 M experiments, with the black lines being the results at 160 °C, dark blue at 180 °C, light blue at 200 °C, green at 250 °C, and red at 350 °C.

in the a/b- and c- direction is shown in Figure 7C. This plot shows that not only the particle size, but also the aspect ratio can be controlled by the synthesis temperature. Generally, the volume weighted crystallite sizes obtained from Rietveld analysis are smaller than the particle sizes obtained in the PDF analysis, but the time and temperature trends of the growth are similar.

The growth mechanisms were further studied by doing kinetic analysis (Lifshitz–Slyszov–Wagner (LSW) theory) of the growth curves in the crystallographic a direction as shown in Figure 8. The expression $D(t) - D_0 = k\cdot(t - t_0)^{1/x}$ was fitted to the growth curves for the 2 M experiments from 160 to 250 °C between 1 and 30 min. D is the particle diameter at time t, D_0 is the diameter at time t_0, while k and x are free variables. The resulting values and fits are shown in Figure 8. x is dependent on the growth mechanism, and the LSW theory states that if the volume of the particles increases linearly with time, then the reaction is limited by diffusion of the precursor, and not by the reaction at the surface of the particles.[47] In this

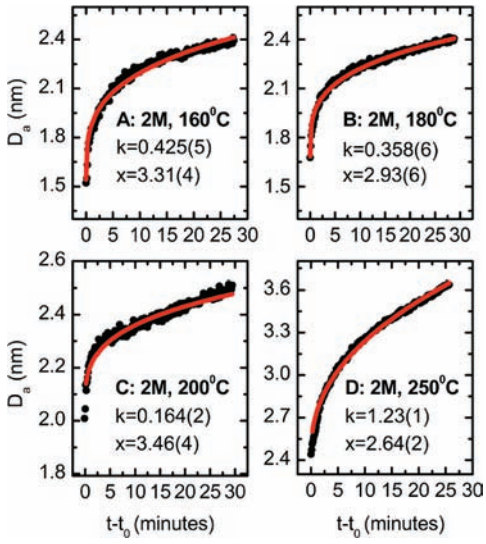

Figure 8. LSW fits to the data for the experiments from 160 to 250 °C with 2 M. The data points are shown as black dots, with the fit as a red line. The expression $D(t) - D_0 = k\cdot(t - t_0)^{1/x}$ was fitted for t between 1 and 30 min. D is the particle diameter in the a direction at time t, D_0 was chosen as the diameter at time t_0 = 1 min, while k and x were free variables.

case, x should take a value of 3, and this is close to the results obtained here. From 160 to 200 °C, the diffusion is expected to be limited by the amount of Sn^{4+} found as $[Sn(OH_2)_{6-y}(OH)_y]^{(4-y)+}$. At higher temperatures, where the growth happens by Ostwald ripening, small particles need to be dissolved to provide precursor for growth of the larger nanoparticles.

Structural Changes of SnO_2. Figure 9A and B shows the changes in unit cell parameters, $c - c_{final}$ and $a - a_{final}$, as a function of the particle size obtained in the Rietveld refinement.

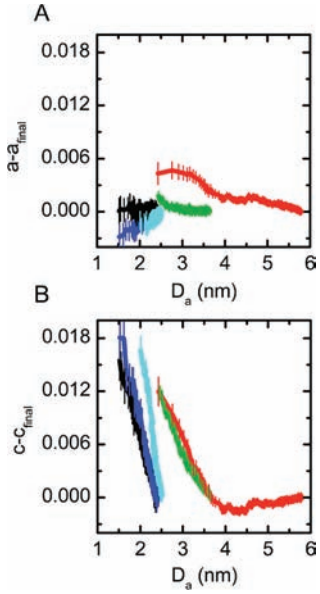

Figure 9. Changes in the unit cell plotted as function of particle size D_a for the 2 M experiments. (A) Changes in the a-axis ($a - a_{final}$). (B) Changes in the c-axis ($c - c_{final}$). The black lines show the results from 160 °C, dark blue are for 180 °C, light blue for 200 °C, green for 250 °C, and the red is for 350 °C.

dx.doi.org/10.1021/ja300978f | J. Am. Chem. Soc. 2012, 134, 6785–6792

Only changes in the parameters within each experiment are considered because the absolute values are somewhat uncertain due to the necessary lack of internal standard in the in situ experiments. As the particles grow, the unit cell decreases along the *c*-direction. This effect is much smaller in the *a*-direction, and the size-dependent structural changes are therefore anisotropic. Expansion of the bulk unit cell in nanoparticles is well-known for many metal oxide systems, and different explanations have been given, such as valence reduction,[48] stacking faults,[23] and surface defect effects.[49] The present in situ data are not of sufficient quality to probe in detail the origin of the unit cell size dependency as reliable values for the precise occupancies and atomic positions cannot be extracted. For further analysis of the size/structure effect, high-quality, low-temperature ex situ X-ray and neutron total scattering data are needed.

The PXRD experiments at MAX-lab provide additional information about the relation between nanosized particles and crystal structure. For the experiments using 1 M, the diffraction peaks are abnormally broad as is especially clear for the (110) peak at ca. 17° shown in Figure 10. For the 180 and 250 °C

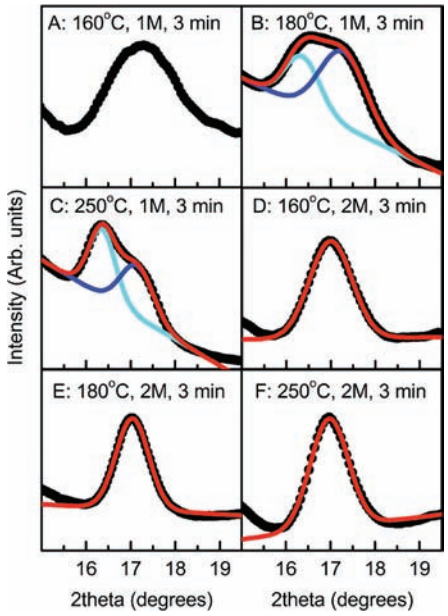

Figure 10. Section of the PXRD frames collected 3 min after initiation of the experiments showing the (110) peaks of the SnO_2 structures. The data points are seen as black dots, and the fitted Gaussian curves are shown as red lines. For the experiments done with 1 M $SnCl_4$ at 180−250 °C, double peaks were observed, and these were fitted with two Gaussians, shown in blue and light blue.

data, the line shape is clearly not symmetric. This could be due to the coexistence of two different polymorphs of SnO_2, the bulk tetragonal phase and an orthorhombic modification. The orthorhombic phase is a high pressure polymorph, and it has been reported to exist in the bulk phase above 5 GPa.[50] The high pressure polymorph has the $CaCl_2$ structure (space group *Pnnm*) and forms through a second-order phase transition from the tetragonal phase. At pressures above 12 GPa, this structure turns into another orthorhombic phase (α-PbO_2 structure), and at even higher pressures a cubic phase becomes stable. Earlier studies of tin oxide nanostructures have reported the formation of the high pressure polymorphs due to the large surface-to-volume ratio of the nanoparticles, elevating the pressure on the particles. However, these studies only show formation of the α-PbO_2 polymorph,[51−54] whereas the $CaCl_2$ structure has not earlier been reported as a stable phase due to size effect.

The bulk phase and the first high pressure phase are closely related, as is seen in the unit cell parameters in Table 1, and

Table 1. Structures of SnO_2

phase	space group	structure type	lattice	unit cell[55]
bulk phase	*P*42/*mnm*	rutile	tetragonal	*a* = 4.737 Å, *b* = 4.737 Å, *c* = 3.186 Å
phase II, HP	*Pnnm*	$CaCl_2$	orthorhombic	*a* = 4.653 Å, *b* = 4.631 Å, *c* = 3.155 Å
phase III, HP	*Pbcn*	α-PbO_2	orthorhomic	*a* = 4.744 Å, *b* = 5.707 Å, *c* = 5.209 Å,
phase IV, HP	$Pa\bar{3}$	distorted flourite	cubic	*a* = 4.888 Å

distinguishing between the two structures is quite difficult due to the large peak broadening and the lack of an internal standard. Therefore, only a crude model with few parameters was used to extract the phase fractions. The weight percent of the orthorhombic/tetragonal phase was therefore roughly estimated by simply fitting Gaussian curves to the (110) peaks and determining the ratio between the two intensities. The results are shown in Figure 11. For the 1 M, 160 °C data, it

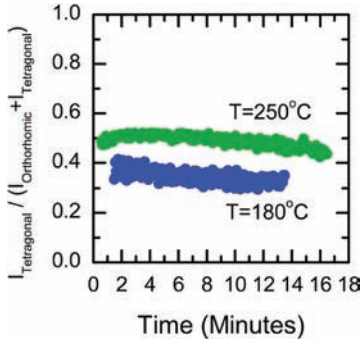

Figure 11. The ratio between the intensity from the tetragonal (110) peak and the sum of the tetragonal and orthorhombic peak intensities.

is not clear whether one or two phases were present; the peak shows slight asymmetry, but it is not possible to get a stable fit using two Gaussian functions. Therefore, the 1 M 160 °C data will not be considered any further. For all of the 2 M data, only the bulk tetragonal rutile phase was present. At 1 M and 180 °C, the tetragonal phase fraction is ∼30%, whereas at 250 °C, this fraction has increased to ∼50%. The fractions are constant throughout the experiments. This shows that by choosing appropriate hydrothermal synthesis parameters, not only the size and the morphology of the nanoparticles can be controlled, but also the specific crystal structure.

■ CONCLUSIONS

The PDF method applied to total scattering data provides information about noncrystalline compounds that cannot be obtained using conventional crystallographic techniques. This opens a huge uncharted territory for in situ studies of chemical

dx.doi.org/10.1021/ja300978f | *J. Am. Chem. Soc.* 2012, 134, 6785−6792

reactions. On the basis of in situ total scattering experiments, the formation mechanism for SnO_2 nanoparticles from aqueous solutions of $SnCl_4$ was established. When dissolving the precursor, both $[SnCl_{6-x}(H_2O)_x]^{(4-x)+}$ and $[Sn(H_2O)_{6-y}(OH)_y]^{(4-y)+}$ are present in the solution, but the SnO_2 nanoparticles crystallize uniquely from Sn^{4+} ions coordinated to H_2O/OH^-. The nanoparticle size and aspect ratio can be controlled by adjusting the precursor concentration, the reaction temperature, and time. The growth is found to be limited by diffusion of precursor to the growing nanoparticle, but only at temperatures above 250 °C do the particles grow by Ostwald ripening. The *c*-axis of the unit cell is found to be dependent on the particle size, and it expands for small particle sizes. The *a*-axis is found to be almost independent of particle size. For very small particles (<4 nm), the high pressure orthorhombic polymorph of SnO_2 is observed ($CaCl_2$ structure). Thus, adjustment of hydrothermal synthesis parameters not only provides control over particle size and morphology, but also over the crystal structure.

■ ASSOCIATED CONTENT

Ⓢ Supporting Information

Details and examples of the refinements of the PDFs (PDFgui and SrFit). Details and examples on the Rietveld refinement and size determination (FullProf). TEM image of SnO_2 nanoparticles. This material is available free of charge via the Internet at http://pubs.acs.org.

■ AUTHOR INFORMATION

Corresponding Author

sb2896@columbia.edu; bo@chem.au.dk

Notes

The authors declare no competing financial interest.

■ ACKNOWLEDGMENTS

This work was supported by The Danish Strategic Research Council (Center for Energy Materials), the Danish National Research Foundation (Center for Materials Crystallography), and the Danish Research Council for Nature and Universe (Danscatt). MAX-lab and the Advanced Photon source, APS, are acknowledged for beamtime. Work in the Billinge group was supported by the U.S. National Science Foundation through grant DMR-0703940. Use of the Advanced Photon Source was supported by the U.S. Department of Energy, Office of Science, Office of Basic Energy Sciences, under contract no. DE-AC02-06CH11357. Dörthe Haase (MAXlab), Kevin Beyer (APS), Peter Nørby (Aarhus University), Jacob Becker (Aarhus University), and Per Runge Christensen (Aarhus University) are thanked for assistance during the experiments.

■ REFERENCES

(1) Kim, C.; Noh, M.; Choi, M.; Cho, J.; Park, B. *Chem. Mater.* **2005**, *17*, 3297.

(2) Ansari, S. G.; Boroojerdian, P.; Sainkar, S. R.; Karekar, R. N.; Aiyer, R. C.; Kulkarni, S. K. *Thin Solid Films* **1997**, *295*, 271.

(3) Burda, C.; Chen, X. B.; Narayanan, R.; El-Sayed, M. A. *Chem. Rev.* **2005**, *105*, 1025.

(4) Daniel, M. C.; Astruc, D. *Chem. Rev.* **2004**, *104*, 293.

(5) Byrappa, K.; Adschiri, T. *Prog. Cryst. Growth Charact.* **2007**, *53*, 117.

(6) Bremholm, M.; Felicissimo, M.; Iversen, B. B. *Angew. Chem., Int. Ed.* **2009**, *48*, 4788.

(7) Lock, N.; Bremholm, M.; Christensen, M.; Almer, J.; Chen, Y. S.; Iversen, B. B. *Chem.-Eur. J.* **2009**, *15*, 13381.

(8) Tyrsted, C.; Becker, J.; Hald, P.; Bremholm, M.; Pedersen, J. S.; Chevallier, J.; Cerenius, Y.; Iversen, S. B.; Iversen, B. B. *Chem. Mater.* **2010**, *22*, 1814.

(9) Mi, J. L.; Christensen, M.; Tyrsted, C.; Jensen, K. O.; Becker, J.; Hald, P.; Iversen, B. B. *J. Phys. Chem. C* **2010**, *114*, 12133.

(10) Lock, N.; Christensen, M.; Jensen, K. M. Ø.; Iversen, B. B. *Angew. Chem., Int. Ed.* **2011**, *50*, 7045.

(11) Mi, J. L.; Jensen, T. N.; Christensen, M.; Tyrsted, C.; Jørgensen, J. E.; Iversen, B. B. *Chem. Mater.* **2011**, *23*, 1158.

(12) Laumann, A.; Jensen, K. M. Ø.; Tyrsted, C.; Bremholm, M.; Fehr, K. T.; Holzapfel, M.; Iversen, B. B. *Eur. J. Inorg. Chem.* **2011**, 2221.

(13) Jensen, K.; Christensen, M.; Tyrsted, C.; Iversen, B. B. *J. Appl. Crystallogr.* **2011**, *44*, 287.

(14) Jensen, K. M. Ø.; Christensen, M.; Tyrsted, C.; Bremholm, M.; Iversen, B. B. *Cryst. Growth Des.* **2011**, *11*, 753.

(15) Chupas, P. J.; Qiu, X. Y.; Hanson, J. C.; Lee, P. L.; Grey, C. P.; Billinge, S. J. L. *J. Appl. Crystallogr.* **2003**, *36*, 1342.

(16) Chupas, P. J.; Chaudhuri, S.; Hanson, J. C.; Qiu, X. Y.; Lee, P. L.; Shastri, S. D.; Billinge, S. J. L.; Grey, C. P. *J. Am. Chem. Soc.* **2004**, *126*, 4756.

(17) Chapman, K. W.; Chupas, P. J.; Kepert, C. J. *J. Am. Chem. Soc.* **2005**, *127*, 11232.

(18) Chupas, P. J.; Chapman, K. W.; Jennings, G.; Lee, P. L.; Grey, C. P. *J. Am. Chem. Soc.* **2007**, *129*, 13822.

(19) Oxford, S. M.; Lee, P. L.; Chupas, P. J.; Chapman, K. W.; Kung, M. C.; Kung, H. H. *J. Phys. Chem. C* **2010**, *114*, 17085.

(20) Zhang, F.; Chupas, P. J.; Lui, S. L. A.; Hanson, J. C.; Caliebe, W. A.; Lee, P. L.; Chan, S. W. *Chem. Mater.* **2007**, *19*, 3118.

(21) Billinge, S. J. L.; Kanatzidis, M. G. *Chem. Commun.* **2004**, 749.

(22) Masadeh, A. S.; Bozin, E. S.; Farrow, C. L.; Paglia, G.; Juhas, P.; Billinge, S. J. L.; Karkamkar, A.; Kanatzidis, M. G. *Phys. Rev. B* **2007**, 76.

(23) Idota, Y.; Kubota, T.; Matsufuji, A.; Maekawa, Y.; Miyasaka, T. *Science* **1997**, *276*, 1395.

(24) Li, N. C.; Martin, C. R.; Scrosati, B. *Electrochem. Solid-State Lett.* **2000**, *3*, 316.

(25) Park, M. S.; Wang, G. X.; Kang, Y. M.; Wexler, D.; Dou, S. X.; Liu, H. K. *Angew. Chem., Int. Ed.* **2007**, *46*, 750.

(26) Paek, S. M.; Yoo, E.; Honma, I. *Nano Lett.* **2009**, *9*, 72.

(27) Courtney, I. A.; Dahn, J. R. *J. Electrochem. Soc.* **1997**, *144*, 2045.

(28) Barsan, N.; Schweizer-Berberich, M.; Gopel, W. *Fresenius' J. Anal. Chem.* **1999**, *365*, 287.

(29) Shanthi, E.; Dutta, V.; Banerjee, A.; Chopra, K. L. *J. Appl. Phys.* **1980**, *51*, 6243.

(30) Fujihara, S.; Maeda, T.; Ohgi, H.; Hosono, E.; Imai, H.; Kim, S. H. *Langmuir* **2004**, *20*, 6476.

(31) Chiu, H. C.; Yeh, C. S. *J. Phys. Chem. C* **2007**, *111*, 7256.

(32) Baik, N. S.; Sakai, G.; Miura, N.; Yamazoe, N. *Sens. Actuators, B* **2000**, *63*, 74.

(33) Sakai, G.; Baik, N. S.; Miura, N.; Yamazoe, N. *Sens. Actuators, B* **2001**, *77*, 116.

(34) Zhang, D. F.; Sun, L. D.; Yin, J. L.; Yan, C. H. *Adv. Mater.* **2003**, *15*, 1022.

(35) Fang, Z.; Assaaoudi, H.; Lin, H. B.; Wang, X. M.; Butler, I. S.; Kozinski, J. A. *J. Nanopart. Res.* **2007**, *9*, 683.

(36) Toledo-Antonio, J. A.; Gutierrez-Baez, R.; Sebastian, P. J.; Vazquez, A. *J. Solid State Chem.* **2003**, *174*, 241.

(37) Ma, J.; Zhang, J.; Wang, S.; Wang, Q.; Jiao, L.; Yang, J.; Duan, X.; Liu, Z.; Lian, J.; Zheng, W. *CrystEngComm* **2011**, *13*, 4.

(38) Lou, X. W.; Wang, Y.; Yuan, C. L.; Lee, J. Y.; Archer, L. A. *Adv. Mater.* **2006**, *18*, 2325.

(39) Becker, J.; Bremholm, M.; Tyrsted, C.; Pauw, B.; Jensen, K. M. Ø.; Eltzholtz, J.; Christensen, M.; Iversen, B. B. *J. Appl. Crystallogr.* **2010**, 43.

(40) Hammersley, A. P.; Svensson, S. O.; Hanfland, M.; Fitch, A. N.; Hausermann, D. *High Pressure Res.* **1996**, *14*, 235.

(41) Farrow, C. L.; Juhas, P.; Liu, J. W.; Bryndin, D.; Bozin, E. S.; Bloch, J.; Proffen, T.; Billinge, S. J. L. *J. Phys.: Condens. Matter* **2007**, *19*, 335219.
(42) Rodriguez-Carvajal, J. *Physica B* **1993**, *192*, 55.
(43) Taylor, M. J.; Coddington, J. M. *Polyhedron* **1992**, *11*, 1531.
(44) Shannon, R. D. *Acta Crystallogr., Sect. A* **1976**, *32*, 751.
(45) Shihada, A. F.; Abushamleh, A. S.; Weller, F. *Z. Anorg. Allg. Chem.* **2004**, *630*, 841.
(46) Guinier, A. *X-ray Diffraction In Crystals, Imperfect Crystals and Amorphous Bodies*; Dover: New York, 1956.
(47) Rao, C. N. R.; Müller, A.; Cheetham, A. K. *Nanomaterials Chemistry*; Wiley-VCHn Verlag GmbH & Co. KGaA: Weinheim, 2007.
(48) Tsunekawa, S.; Ishikawa, K.; Li, Z. Q.; Kawazoe, Y.; Kasuya, A. *Phys. Rev. Lett.* **2000**, *85*, 3440.
(49) Li, G. S.; Boerio-Goates, J.; Woodfield, B. F.; Li, L. P. *Appl. Phys. Lett.* **2004**, *85*, 2059.
(50) Suito, K.; Kawai, N.; Masuda, Y. *Mater. Res. Bull.* **1975**, *10*, 677.
(51) Chen, Y.; Campbell, L.; Zhou, W. L. *J. Cryst. Growth* **2004**, *270*, 505.
(52) Cukrov, L. M.; McCormick, P. G.; Galatsis, K.; Wlodarski, W. *Sens. Actuators, B* **2001**, *77*, 491.
(53) Nayral, C.; Viala, E.; Fau, P.; Senocq, F.; Jumas, J. C.; Maisonnat, A.; Chaudret, B. *Chem.-Eur. J.* **2000**, *6*, 4082.
(54) Dai, Z. R.; Gole, J. L.; Stout, J. D.; Wang, Z. L. *J. Phys. Chem. B* **2002**, *106*, 1274.
(55) Haines, J.; Leger, J. M. *Phys. Rev. B* **1997**, *55*, 11144.